engineering proceedings

MDPI

Proceeding Paper

Galileo Performance Improvements Employing Meta-Signals—Robustness Analysis against Payload and Receiver Distortions †

Florian C. Beck [1,2,*], Christoph Enneking [1], Steffen Thölert [1,2] and Michael Meurer [1,2]

[1] Institute for Communications and Navigation, German Aerospace Center (DLR), Münchener Str. 20, 82234 Wessling, Germany; christoph.enneking@dlr.de (C.E.); steffen.thoelert@dlr.de (S.T.); michael.meurer@dlr.de (M.M.)
[2] Chair of Navigation, RWTH Aachen University, Mies-van-der-Rohe-Str. 15, 52074 Aachen, Germany
* Correspondence: florian.beck@dlr.de
† Presented at the European Navigation Conference 2023, Noordwijk, The Netherlands, 31 May–2 June 2023.

Abstract: A concept that has been explored as a means to obtain decimeter-level positioning accuracy with global navigation satellite systems (GNSSs) is meta-signal processing (MSP), which treats several stand-alone GNSS signals as a single composite wideband signal. BeiDou Navigation Satellite System (BDS) III already offers with the B1I+B1C signal a meta-signal, while the forthcoming Galileo (GAL) E1D could be combined with E1B or E1C if the E1D signal is broadcast with a frequency offset to the L1/E1 carrier frequency. This would boost the ranging performance of GAL open service (OS) in the upper L-band through MSP. However, the cross-correlation function (CCF) of meta-signals contain numerous high side-maxima which can, when wrongly identified as the main peak, lead to significant pseudo-range errors of multiple meters. The probability of such a false lock is known to increase with decreasing signal-to-noise ratios but can significantly increase even further due to imperfections in the analog hardware components (e.g., linear and non-linear effects of a high-power amplifier (HPA), an output multiplexer (OMUX), a transmitter filter, and a front-end receiver), as these can distort the CCF. One remaining question is whether meta-signals are a well-suited approach to reliably increase ranging performance in the presence of payload and receiver distortions. This study presents the first systematic assessment of the robustness of several potential meta-signal options enabled by a forthcoming GAL E1D signal for different levels of distortion. The results show significant performance gains but also indicate constraints regarding the choice of signals when considering MSP under the influence of distortions.

Keywords: GNSS; Galileo; meta-signal processing; dual-band tracking

Citation: Beck, F.C.; Enneking, C.; Thölert, S.; Meurer, M. Galileo Performance Improvements Employing Meta-Signals —Robustness Analysis against Payload and Receiver Distortions. *Eng. Proc.* **2023**, *54*, 4. https://doi.org/10.3390/ENC2023-15472

Academic Editors: Tom Willems and Okko Bleeker

Published: 29 October 2023

1. Introduction

In recent decades, an evolving global navigation satellite system (GNSS) receiver landscape fueled the discussion of further introductions of new GNSS signals to meet emerging market needs. For instance, Galileo (GAL) E5-AltBOC and BeiDou Navigation Satellite System (BDS) B2-ACEBOC were added to the signal portfolio to offer a signal with increased bandwidth and therefore higher-ranging capabilities in the lower L-band. Options to broadcast new broadband signals in the upper L-band are limited due to spectrum restrictions as well as possible intra- and inter-system interference issues. In the upper L-band, a wideband open service (OS) ranging signal is missing, but to meet market demands, the introduction of a quasi-pilot signal for low-complexity receivers [1–3] with a potential offset to the L1 carrier was proposed by previous studies [4–6]. Adding this new signal with a frequency offset may enable meta-signal processing (MSP) of the GAL E1B/C with the E1D signal. The concept of MSP was first discussed in the context that a GNSS transmits a multitude of satellite navigation (satnav) signals across multiple

frequencies [7,8]. MSP aims to track a combination of ranging signals which have different carrier frequencies and therefore have a larger Gabor bandwidth, which can in theory greatly increase tracking performance [9,10].

However, meta-signals have a severe ambiguity problem since their auto-correlation functions (ACFs) contain a large number of side-peaks which leads to larger probabilities of false locks in high-noise regimes [11]. To solve this issue, research has focused on developing tracking algorithms that optimize the benefits of meta-signals in particular for the BDS III signals in the upper L-band [10]. Notably, the extension of the double estimator/double phase estimator [12,13] and the wideband high-accuracy joint tracking technique [14] have been developed to improve the tracking performance of the BDS B1I-B1C meta-signal while reducing the number of required correlators [15].

The theoretical gains in terms of ranging performance and the mitigation of the ambiguity problem were the subject of previous work [9]. In [16], Nardin et al. conducted a first analysis of cross-correlation function (CCF) property changes in the presence of linear distortions. This study was limited to a meta-signal comprising a binary offset carrier (BOC)(1,1) and binary phase-shift keying (BPSK)(1)/BOC(1,1) with a frequency offset of 12×1.023 MHz. However, there is a lack of further findings regarding the influence of distortions on MSP performance dependent on the modulation and chosen frequency offset. In this paper, we present an extended analysis through a systematic assessment of the robustness of the time of arrival (TOA) estimation error standard deviation (stdev.) of several potential meta-signal options enabled by a forthcoming GAL E1D signal for different levels of distortions caused by a transmitter and a receiver. The results suggest that MSP may enable an improvement in the ranging performance depending on the exact shape and placement of the GAL E1D signal. Certain GAL E1D signal options were found to be sub-optimal in the context of MSP since the ambiguity problem is elevated in the presence of distortions.

2. System Model

2.1. Transmitter and Channel

The payload and channel of the system model consist of four building blocks, namely the input multiplexer (IMUX), high-power amplifier (HPA), output multiplexer (OMUX), and channel, as illustrated in Figure 1.

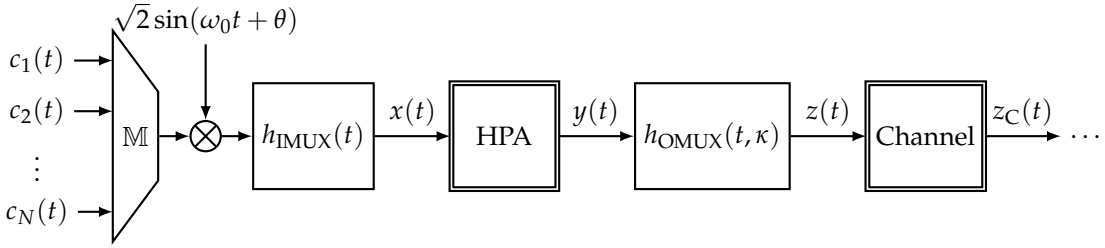

Figure 1. System model of transmitters and channels.

The IMUX $\mathbb{M}$ composes N analog code-division multiple access (CDMA) waveforms $c_n(t) = \sum_{m=-\infty}^{+\infty} c_n[m] d_n[m] p_n(t - mT_{\mathrm{c},n})$ to one composite signal

$$x(t) = h_{\mathrm{IMUX}}(t) * \left(\mathbb{M}\{c_1(t), c_2(t), ..., c_N(t) | \boldsymbol{p}, \boldsymbol{\phi}, \boldsymbol{f}^{\Delta}\} e^{j\omega_0 t} \right) \tag{1a}$$

$$= h_{\mathrm{IMUX}}(t) * \left(\left(\sum_{n=1}^{N} c_n(t) \sqrt{P_n} e^{j\phi_n} e^{j2\pi f_n^{\Delta} t} + x_{\mathrm{IM}}(t) \right) e^{j\omega_0 t} \right) \tag{1b}$$

modulated onto a joint carrier with the angular frequency $\omega_0 = 2\pi f_0$, where $c_n[m] \in \{+1, -1\}$ denotes the binary spreading code with a code rate of $f_{\mathrm{c},n} = 1/T_{\mathrm{c},n}$, $d_n[m] \in \{+1, -1\}$ denotes the navigation data, and $p_n(t)$ denotes the pulse shape of the n-th CDMA waveform. Furthermore, $f_n^{\Delta} = f_0 - f_n$ denotes the frequency offset of the

n-th CDMA waveform to the carrier frequency. In the case of the GAL E1 band, the first three CDMA waveforms are the BOC-modulated PRS and the composite binary offset carrier (CBOC)-modulated E1B and E1C signals. The fourth CDMA waveform was the potential E1D signal generated with a frequency offset. Possible imperfections in the digital-to-analog conversion may be captured by the filter $h_{\mathrm{IMUX}}(t)$. However, in the following, an all-pass IMUX was assumed. The multiplexed pass-band signal $x(t)$ was then fed to an HPA which amplifies the signal to a desired output power level. In this study, we constrain ourselves to an idealized, memoryless HPA model such that the resulting amplified signal is

$$y(t) = A(|x(t)|)e^{i(\Phi(|x(t)|)+\mathrm{atan2}(\mathrm{Im}\{x(t)\},\mathrm{Re}\{x(t)\}))} \tag{2}$$

where $A(|x(t)|)$ denotes the AM/AM mapping function and $\Phi(|x(t)|)$ denotes the AM/PM mapping function [17]. The amplified signal $y(t)$ is then passed to the OMUX which facilitates a band limitation, which can be modeled with a filter such that the signal radiated from the satellite can be expressed as

$$z(t) = h_{\mathrm{OMUX}}(t, \kappa) * y(t) \tag{3}$$

where $\kappa \in [0, 1]$ denotes the payload distortion parameter, which controls the degree of filtering distortion introduced by the OMUX. Section 2.3 describes the implementation of a scalable distortion OMUX filter $h_{\mathrm{OMUX}}(t, \kappa)$ used in the numerical evaluations. After OMUX filtering, the satellite contribution

$$z_{\mathrm{C}}(t) = \gamma z(t - \tau_0) \tag{4}$$

is formed by the channel which delays the signal by τ_0 and attenuates the signals mainly due to path loss, which is captured by a constant complex scalar γ.

2.2. Receiver

A straight-forward receiver model may assume an introduction of additive white Gaussian noise (AWGN) $\xi(t)$ onto the pass-band signal $z_{\mathrm{C}}(t)$ on the ground before its demodulation with $\omega_{\mathrm{IF}} = 2\pi f_{\mathrm{IF}}$ and front-end filtering with a ideal brick-wall filter $h_{\mathrm{FE}}(t) = B\sin(\pi Bt)/(\pi Bt) \triangleq B\,\mathrm{sinc}(Bt)$, where B denotes the two-sided front-end filtering bandwidth, resulting in the analog receive signal $r(t)$. This receive signal is then digitized using a sampling rate of $1/T_s$, resulting in the receive signal vector:

$$\boldsymbol{r} = \begin{bmatrix} r(0) & r(T_s) & r(2T_s) & \cdots & r((N_s-1)T_s) \end{bmatrix}^{\mathrm{T}} \quad \in \mathbb{C}^{N_s \times 1} \tag{5}$$

where N_s denotes the number of samples accumulated for a specific integration time and $(.)^{\mathrm{T}}$ denotes the transpose operator. Applying the receive signal vector $\boldsymbol{r}$ to a correlator bank

$$\boldsymbol{C} = \begin{bmatrix} \bar{\boldsymbol{c}}^{(0)} & \bar{\boldsymbol{c}}^{(1)} & \cdots & \bar{\boldsymbol{c}}^{(n_c)} & \cdots & \bar{\boldsymbol{c}}^{(N_c-1)} \end{bmatrix} \quad \in \mathbb{C}^{N_s \times N_c}, \tag{6}$$

where $\bar{\boldsymbol{c}}^{(n_c)}$ denotes the vectorized signal replica $\bar{c}(t - \tau_{n_c})$ with the shift $\tau_{n_c} = \Delta((N_c - 1)/2 + n_c)$ using the uniform correlator spacing Δ, yields then a noisy, sampled CCF $\tilde{\boldsymbol{q}} = \boldsymbol{C}^{\mathrm{H}}\boldsymbol{r} \in \mathbb{C}^{N_c \times 1}$ for a specific noise realization of $\xi(t)$. Figure 2 shows the generation of the correlator output $\tilde{\boldsymbol{q}}$ for the straight-forward model.

For simulation purposes, it is convenient to replace the straight-forward receiver model with an equivalent alternative, shown in Figure 3, which adds colored noise $\tilde{\boldsymbol{n}}$ directly onto the noise-free version, a sampled CCF $\boldsymbol{q} = \boldsymbol{C}^{\mathrm{H}}\boldsymbol{s} \in \mathbb{C}^{N_c \times 1}$ resulting in a noisy CCF $\tilde{\boldsymbol{q}}$ with identical statistical properties as in the straight-forward model. For the simulation, a vector for different noise power levels has to be computed based on the carrier-to-noise-density ratio (C/N_0) that is to be investigated. The advantage of this approach is that the Monte-

Carlo simulation can be achieved with less computational effort since $N_s \gg N_c$. From a statistical viewpoint, the system models shown in Figures 2 and 3 are fully equivalent. This is established in the following theorem.

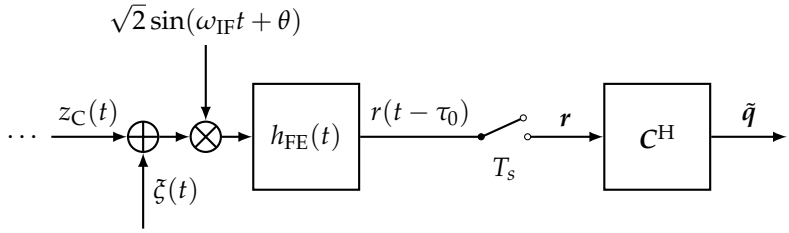

Figure 2. Straight-forward system model of the receiver with the addition of white noise onto a pass-band signal.

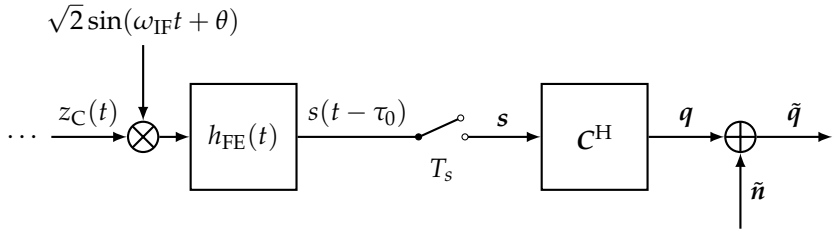

Figure 3. Alternative system model of the receiver with the addition of colored noise onto a noise-free correlator output.

Theorem 1. *The addition of the colored noise in the post-correlation domain is statistically equivalent to the addition of noise in the pre-correlation domain when generating the zero mean colored noise vector* $\tilde{\boldsymbol{n}} = \boldsymbol{D}^{\mathrm{H}}\boldsymbol{\eta}$ *using a white noise vector* $\boldsymbol{\eta} \sim \mathcal{CN}(0, \sigma^2\mathbf{I})$ *with* $\sigma^2 = N_0 B$ *and a coloring matrix* $\boldsymbol{D}$*. The coloring matrix* $\boldsymbol{D}$ *is derived from the covariance matrix* $\boldsymbol{\Sigma} = E[\tilde{\boldsymbol{q}}\tilde{\boldsymbol{q}}^{\mathrm{H}}] = \boldsymbol{C}^{\mathrm{H}}\boldsymbol{W}\boldsymbol{C}$ *with*

$$\boldsymbol{e}_i^{\mathrm{T}}\boldsymbol{W}\boldsymbol{e}_j = \mathrm{sinc}(BT_s(i-j)) \quad \forall i,j \in \{0,...,N_s-1\} \tag{7}$$

and by applying the eigendecomposition (ED) of

$$\boldsymbol{\Sigma} = \boldsymbol{Q}\boldsymbol{\Lambda}\boldsymbol{Q}^{-1} = \boldsymbol{Q}\boldsymbol{\Lambda}^{\frac{1}{2}}\left(\boldsymbol{\Lambda}^{\frac{1}{2}}\right)^{\mathrm{H}}\boldsymbol{Q}^{\mathrm{H}} \triangleq \boldsymbol{D}^{\mathrm{H}}\boldsymbol{D} \tag{8}$$

exploiting $\boldsymbol{Q}^{-1} = \boldsymbol{Q}^{\mathrm{H}}$*, and defining the coloring matrix as* $\boldsymbol{D} = \left(\boldsymbol{Q}\boldsymbol{\Lambda}^{\frac{1}{2}}\right)^{\mathrm{H}}$.

Proof of Theorem 1. The vectorized receive signal can be expressed as

$$\boldsymbol{r} = \boldsymbol{s} + \boldsymbol{n} \quad \text{with} \quad \boldsymbol{n} \sim \mathcal{CN}(0, \sigma^2\boldsymbol{W}) \tag{9}$$

where $\sigma^2 = N_0 B$ and its covariance matrix $\boldsymbol{W} \in \mathbb{R}^{N_s \times N_s}$ with its matrix entries as defined in Equation (7) accounts for the band-limitation introduced by the front-end filter $h_{\mathrm{FE}}(t)$ [18]. Hence, the received signal $\boldsymbol{r} \sim \mathcal{CN}(\boldsymbol{s}, \sigma^2\boldsymbol{W})$ follows a non-zero mean and non-Gaussian distribution. The noisy correlator output $\tilde{\boldsymbol{q}} = \boldsymbol{C}^{\mathrm{H}}\boldsymbol{r}$ can be expressed as

$$\tilde{\boldsymbol{q}} \sim \mathcal{CN}(\boldsymbol{C}^{\mathrm{H}}\boldsymbol{s}, \sigma^2\boldsymbol{C}^{\mathrm{H}}\boldsymbol{W}\boldsymbol{C}) \tag{10}$$

such that the statistical properties of the colored noise $\tilde{\boldsymbol{n}}$ to be added into the post-correlation domain become evident and we can define

$$\tilde{\boldsymbol{q}} = \boldsymbol{q} + \tilde{\boldsymbol{n}} \quad \text{with} \quad \tilde{\boldsymbol{n}} \sim \mathcal{CN}(0, \sigma^2\boldsymbol{\Sigma}) \tag{11}$$

where $\mathbf{\Sigma} = \boldsymbol{C}^{\mathrm{H}}\boldsymbol{W}\boldsymbol{C}$ and $\boldsymbol{q} = \boldsymbol{C}^{\mathrm{H}}\boldsymbol{s}$. Since $\mathbf{\Sigma}$ is Hermitian and positive-definite, its ED can be expressed as $\mathbf{\Sigma} = \boldsymbol{Q}\mathbf{\Lambda}\boldsymbol{Q}^{\mathrm{H}}$, where $\boldsymbol{Q}$ denotes the matrix of column-wise collected eigenvectors and $\mathbf{\Lambda}$ denotes the diagonal matrix with the eigenvalues. This expression can be reformulated such that we have for the covariance matrix $\mathbf{\Sigma} = \boldsymbol{D}^{\mathrm{H}}\boldsymbol{D}$, as defined in Equarion (8). The, using the coloring matrix $\boldsymbol{D}$ and an AWGN noise vector $\boldsymbol{\eta} \sim \mathcal{CN}(0, \sigma^2\mathbf{I})$ to generate the colored noise vector $\tilde{\boldsymbol{n}} = \boldsymbol{D}^{\mathrm{H}}\boldsymbol{\eta}$ achieves the correct statistical properties of $\tilde{\boldsymbol{q}}$ as the covariance matrix is

$$\mathrm{cov}(\tilde{\boldsymbol{q}}, \tilde{\boldsymbol{q}}) = E[(\tilde{\boldsymbol{q}} - E[\tilde{\boldsymbol{q}}])(\tilde{\boldsymbol{q}} - E[\tilde{\boldsymbol{q}}])^{\mathrm{H}}] = E[(\tilde{\boldsymbol{q}} - \boldsymbol{q})(\tilde{\boldsymbol{q}} - \boldsymbol{q})^{\mathrm{H}}] \tag{12a}$$

$$= E[\tilde{\boldsymbol{n}}\tilde{\boldsymbol{n}}^{\mathrm{H}}] = E[\boldsymbol{D}^{\mathrm{H}}\boldsymbol{\eta}\boldsymbol{\eta}^{\mathrm{H}}\boldsymbol{D}] = \boldsymbol{D}^{\mathrm{H}}E[\boldsymbol{\eta}\boldsymbol{\eta}^{\mathrm{H}}]\boldsymbol{D} = \sigma^2\boldsymbol{D}^{\mathrm{H}}\boldsymbol{D} = \sigma^2\mathbf{\Sigma}. \tag{12b}$$

□

2.3. Scalable Filtering Distortion

The "morphing" between L states of payload distortion is achieved with a sinusoidal weight function $\boldsymbol{w}(\kappa, L) = [w_1(\kappa, L), ..., w_L(\kappa, L)]^{\mathrm{T}}$, where the l-th element is defined as

$$w_l(\kappa, L) = \begin{cases} \frac{1}{2}\cos(\Omega(L)(\kappa - m(l, L)) + \frac{1}{2} & \text{if } |\kappa - m(l, L)| \leq \frac{1}{L-1} \\ 0 & \text{else} \end{cases} \tag{13}$$

with $\Omega(L) = 2\pi(L-1)$ and $m(l, L) = (l-1)/(L-1)$. A filter with scalable distortions can be then described as

$$H(f, \kappa, \mathcal{H}) = \sum_{l=1}^{L} w_l(\kappa, L)H_l(f) = \boldsymbol{H}(f)\boldsymbol{w}(\kappa, L) \tag{14}$$

with $\kappa \in [0, 1]$ being the distortion scaling coefficient; $L = |\mathcal{H}|$; and the set of ordered filter functions $\mathcal{H} = \{H_1(f), ..., H_L(f)\}$, where $H_1(f)$ is the filter applying the least distortions (e.g., "all-pass" filter), $H_L(f)$ is the filter with maximal distortions, and the filters from $H_2(f)$ to $H_{L-1}(f)$ show an increase in filtering distortion in terms of band limitation and group delay. The scalable distortion OMUX filter in this study uses $L = 5$ filters. The first filter $H_1(f) = 1$ has an all-pass characteristic. The last filter $H_5(f)$ is generated through a polynomial fitting of a measured transfer characteristic of a GNSS satellite payload. $H_2(f)$ and $H_3(f)$ have a pre-distorted Butterworth characteristic of fourth and sixth order, respectively. Furthermore, $H_2(f)$ has two sides with 61.38 MHz and $H_3(f)$ has the same bandwidth as $H_5(f)$. Lastly, $H_4(f)$ is a pre-distorted version of $H_5(f)$, resulting in the same amplitude response but an all-zero phase response.

3. Signal Candidates

In the past, multiple potential signals were proposed to be transmitted as a future GAL E1D signal. In the early 2010s, E1D candidates with no offset to the already transmit signal were the subject of discussions [2,8]. In the second half of the decade, E1D signal candidates with an offset to the carrier of the E1B, E1C, and PRS signals were proposed and investigated [4–6,11,16]. Inspired by the aforementioned proposals, seven E1D signal candidates are investigated in the following, which are either BPSK-rectangular (R), CBOC, or BOC-modulated and have different chipping rates and carrier frequency placements within the upper L-band. The detailed parameters of the signal candidates can be found in Table 1. The spectral allocations of the main lobes and signal carrier placement of the E1D candidates, which where already suggested in earlier studies [5], are either slightly above or below the upper main lobe of the modernized authorized services provided by GAL and other GNSS to avoid inter- and intra-system interference. The signal candidates E1D-a/b/c have 4 × 1.023 MHz, E1D-g has 12 × 1.023 MHz, and E1D-d/e/f have 20 × 1.023 MHz center frequency offsets with respect to the L1/E1 carrier frequency. The most likely modulation for an E1D signal is BPSK-R due to its simplicity suited for reception by low-

complexity receivers. The CBOC and BOC-modulated candidates were included due to interesting ACF properties when assuming a coherent signal generation. The shape of the meta-signal E1C+E1D ACFs is illustrated by Figure 4b. The complex E1C+E1D meta-signal replicas for the simulations are defined as

$$\bar{c}_n(t) = c_{\mathrm{E1C}}(t)e^{-j\pi f_n^{\Delta} t} + c_{\mathrm{E1D}}(t)e^{+j\pi f_n^{\Delta} t}\,. \tag{15}$$

Table 1. Parameters of investigated Galileo E1D signal candidates forming a meta-signal with the Galileo E1C signal.

Candidate	Modulation	$f_{c,\mathrm{E1D}}$/MHz	f^{Δ}/MHz	$f_0 + f^{\Delta}$/MHz	f_{IF}/MHz
E1D-a	BPSK-R	1.0230	4.092	1579.512	1577.466
E1D-b	BPSK-R	0.5115	4.092	1579.512	1577.466
E1D-c	CBOC(6,1,1/11,-)	1.0230	4.092	1579.512	1577.466
E1D-d	BPSK-R	1.0230	20.460	1595.880	1585.650
E1D-e	BPSK-R	0.5115	20.460	1595.880	1585.650
E1D-f	CBOC(6,1,1/11,-)	1.0230	20.460	1595.880	1585.650
E1D-g	BOC(8,1)	1.0230	12.276	1587.696	1581.558

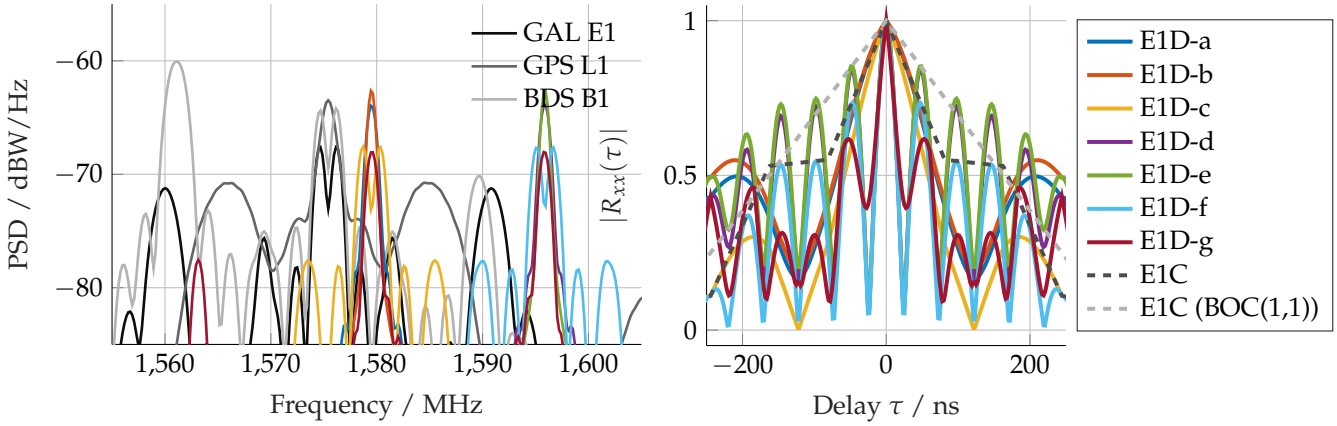

(**a**) (**b**)

Figure 4. Spectral allocation of individual signals and potential Galileo meta-signal ACFs options. (**a**) PSDs of broadcast GNSS L1/E1/B1 signals and potential E1D signal candidates in upper L-band. (**b**) Absolute part of E1C+E1D meta-signal ACFs assuming a centrally placed intermediate frequency.

4. Performance Measures

The first performance metric is the spectral separation coefficient (SSC) [19]

$$\mathrm{SSC}(G_1, G_2, B) = \frac{\int_{-B/2}^{+B/2} G_1(f)G_2(f)\mathrm{d}f}{\int_{-\infty}^{+\infty} G_1(f)\mathrm{d}f \int_{-\infty}^{+\infty} G_2(f)\mathrm{d}f}\,, \tag{16}$$

where $G_1(f)$ and $G_2(f)$ denote the power spectral densities (PSDs) of two signals to test. The second performance measure was the multipath error envelope assuming one line-of-sight (LOS) tap and one non-line-of-sight (NLOS) tap with a 3 dB attenuation for varying multipath tap delays [20]. The last investigated performance measure is the unsmoothed TOA estimation error stdev.

$$\sigma = \sqrt{\frac{1}{J}\sum_{j=1}^{J}(\hat{\tau}_0(j) - \mu)^2} \tag{17}$$

of the code phase, where $\hat{\tau}_0(j)$ denotes the j-th TOA estimate based on the j-th realization of $\tilde{\boldsymbol{q}}$ of, in total, J Monte-Carlo realizations, and $\mu = (1/J)\sum_{j=1}^{J}\hat{\tau}_0(j)$ denotes the sample mean of the TOA estimates, which are derived either by coherent early–late processing (CELP) or noncoherent early–late processing (NELP), as explored in [21].

5. Numerical Results

5.1. Simulation Parameters

The average power of the candidate meta-signals and current signals on the ground is set to −154.0 dBW by assuming an ideal HPA with an average output power of 15.0 dBW and a total propagation loss of 169.0 dB, accounting for path loss, implementation losses, and antenna gains. The power ratio between the E1C and E1D candidates was set to 1:1. The two-sided front-end filtering bandwidth B is 51.150 MHz. The integration time was 1.955 µs. The number of Monte-Carlo runs J for each data point is 200,000. No smoothing for the TOA estimation is assumed. The delay τ_0 was randomized in an interval $[-\frac{1}{3}T_{\mathrm{c,BPSK-R(1)}}, +\frac{1}{3}T_{\mathrm{c,BPSK-R(1)}}]$ to introduce scalloping losses [21]. Non-linear effects introduced by the HPA and an analog-to-digital converter are beyond the scope of this paper. The correlator banks have a spacing of $\Delta_n = T_{\mathrm{c},n}/250$ and $N_c = 501$. The TOA estimation of $\hat{\tau}_0$ uses a parabolic interpolation around the highest value of the absolute and real parts of the CCF vector $\tilde{\boldsymbol{q}}$ using an interpolation equation from [22].

5.2. Spectral Separation Analysis Using the Spectral Separation Coefficient

The self-SSCs of the already broadcast CDMA waveforms in the upper L-band range from −61.9 to −73.1 dB/Hz, assuming a 51.150 MHz two-sided reception bandwidth B. The SSCs between the civilian/OS signals range from −67.9 to −68.3 dB/Hz. The SSCs between the authorized signals range from −72.4 to −88.2 dB/Hz. Table 2 reports the expected SSCs for the currently present CDMA waveforms and the E1D signal candidates with the respective frequency offsets. The signal candidates E1D-a/b/c/g would interfere the most with the BPSK-R(10) waveform as their spectra have a significant overlap. In terms of the SSC, an introduction of the E1D-d/e/f would cause less interference. Among those, the CBOC-modulated E1D-f candidate performs the poorest. Among all investigated candidates, the E1D-e variant would cause the least interference with the already present CDMA waveforms.

Table 2. Spectral separation coefficients in dB/Hz of currently transmitted waveforms (with $f_0 = 1575.42$ MHz) with the investigated added E1D signal candidates within the upper L-Band placed off-center.

	E1D-a	**E1D-b**	**E1D-c**	**E1D-d**	**E1D-e**	**E1D-f**	**E1D-g**
BPSK-R(1)	−82.08	−85.09	−81.58	−96.06	−99.07	−94.91	−87.78
Sine BOC(1,1)	−82.08	−85.09	−75.31	−96.06	−99.07	−89.13	−87.78
MBOC(6,1,1/11)	−81.58	−84.59	−75.53	−94.91	−97.92	−89.19	−86.57
BPSK-R(10)	−72.59	−72.55	−72.85	−96.06	−99.07	−89.14	−76.59
Sine BOC(10,5)	−81.79	−82.12	−79.59	−96.06	−99.07	−90.30	−83.35
Cosine BOC(15,2.5)	−94.91	−96.49	−89.98	−87.13	−90.14	−80.70	−87.36
Sine BOC(14,2)	−90.07	−93.08	−84.60	−91.11	−94.12	−80.86	−87.65

5.3. Multipath Error Envelope

Figure 5 shows the multipath error envelopes of the meta-signals and current GAL signals when assuming an all-pass transmit characteristic, NELP with an early–late spacing $\Delta = 0.01 \times T_{\mathrm{c,BPSK-R(1)}}$, and a 24.552 MHz brick-wall receive filter centrally placed at f_{IF}. The meta-signal using E1D-b/e with the longer chip duration has a poorer multipath rejection than the other signal candidates as the envelope is non-zero up to approximately 586 m in multipath tap length. The meta-signal combinations E1C+E1D-a/b/c/g perform poorer than using the E1C signal as a stand-alone signal in the region from 0 to 50 meters of NLOS tap length. The other meta-signals with E1D-d/e/f have a tighter multipath envelope

but possess more ripples than the current signals' envelopes. According to these results, choosing a larger frequency offset would be beneficial for an E1D signal. Two-correlator NELP of a E1C+E1D-d/e/f signal can reduce the influence of multipath, but due to the sheer number of side peaks in the ACF, an oscillating multipath error can be observed up to the longer of the two chip durations of the stand-alone signals constituting the meta-signal. The minima of this oscillating multipath error of the E1C+E1D-a/b/c/d/e/f meta-signal are approximately located at $1/f^{\Delta}$.

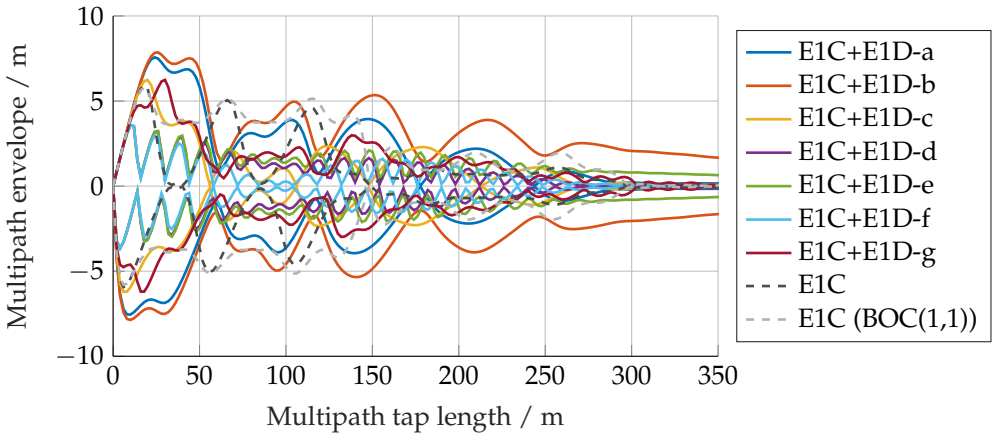

Figure 5. Multipath envelopes of investigated meta-signals assuming a very narrow NELP with an early–late spacing $\Delta = 0.01 \times T_{\mathrm{c,BPSK-R(1)}}$ and the application of a brick-wall filter with a two-sided bandwidth of 24.552 MHz.

5.4. Tracking Performance

Assessing the tracking performance in terms of unsmoothed TOA estimation error stdev. for a fixed C/N_0 is, in this study, the primary performance measure used to judge whether a potential E1D signal may also be a good candidate considering MSP. The carrier power $C = \boldsymbol{s}^{\mathrm{H}}\boldsymbol{s}/N_s$ is derived for each signal to individually test that a fair-ranging performance evaluation for each signal is achieved. However, when directly comparing the status quo tracking, for instance, the GAL E1C signal at a certain noise power N_0B with MSP of a potential E1C+E1D signal, one should keep in mind whether an E1D signal would be added with a 1:1 power ratio with respect to the E1C signal; the combined meta-signal's power would be 3 dB higher than the E1C signal alone, resulting in a boost of TOA estimation error stdev., where the degree depends on the reception situation in terms of noise regime but also the chosen E1D signal.

Figure 6 illustrates the code-phase ranging performance of each investigated signal for the two extreme cases, where either an ideal all-pass payload ($\kappa = 0$) or a realistic distortion of a measured filter is applied ($\kappa = 1$) during the signal formation. In the low-noise regime ($C/N_0 \geq 50$ dB-Hz), two performance tiers of signals can be identified. The meta-signals with the larger frequency offset (E1C+E1D-d/e/f/g) lead to a decreased TOA estimation error stdev. and therefore an increased ranging performance compared to E1C tracking at the same C/N_0. The E1C+E1D-g signal candidate accumulates deformations due its wider bandwidth and experiences the greatest ranging performance degradation for a realistic payload characteristic in comparison to an all-pass payload scenario. The E1C+E1D-f performs best above 45 dB-Hz and sees a performance difference between ideal and fully distorted payload in a transition region from 42 to 47 dB-Hz.

Tracking E1C+E1D-a/b meta-signals is worse than CBOC-tracking of the E1C signal in the all-pass case but even more so for the realistic payload case for a C/N_0 greater than 45 dB-Hz. In the fully distorted case, E1C+E1D-a/b-tracking is worse than BOC-tracking of an E1C signal above 50 dB-Hz C/N_0. Tracking E1C+E1D-a/b instead of E1C only would merely be improved due to the increased signal power but not due to MSP as the ACF main peak is less sharp than that of E1C using a CBOC replica.

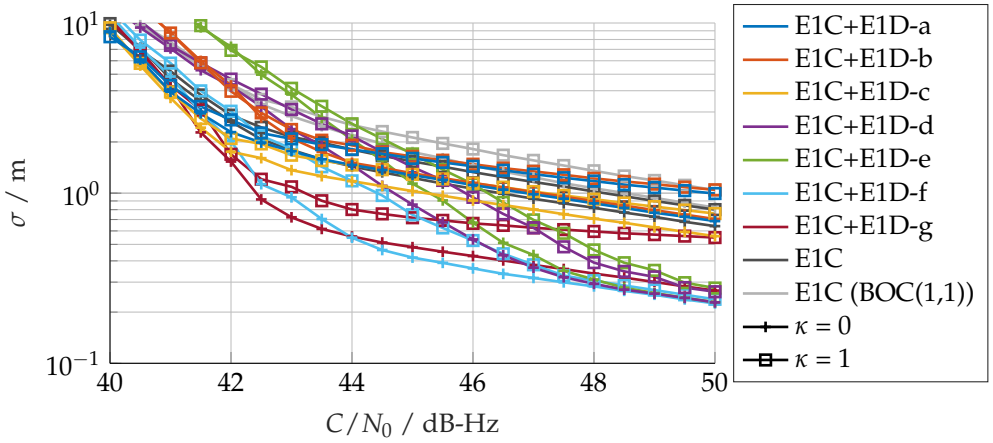

Figure 6. Unsmoothed TOA estimation error stdev. for different noise levels for the two extreme distortion cases for NELP.

Figure 7 shows the evolution of the stdev. and sample mean when varying the distortion parameter κ from 0 to 1 for a fixed C/N_0 of 45 dB-Hz.

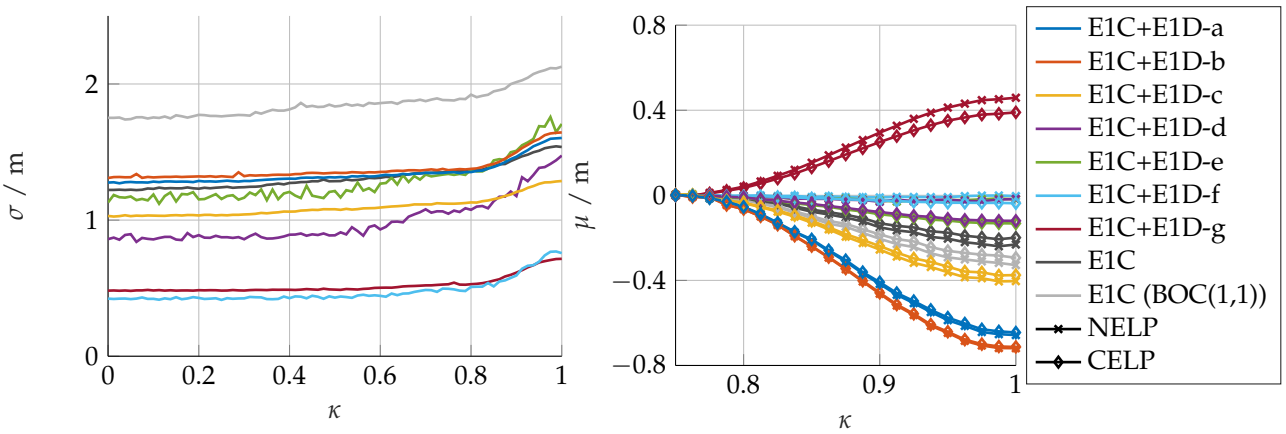

(**a**) (**b**)

Figure 7. Evolution of first and second statistical moments for a fixed noise level of 45 dB-Hz. (**a**) NELP TOA estimation error sample stdev. (**b**) TOA estimation error sample mean.

The gradual increase in band limitation only slightly worsens the TOA estimation error stdev. For $\kappa > 0.75$, the influence of the measured phase response influences the mean and stdev., resulting in a range bias but also a worsening of ranging performance due to the introduced CCF asymmetry.

6. Conclusions

In the near future, MSP of the GAL E1B/C with an E1D signal could lead to significant performance gains for civil GNSS receivers in the upper L-band. The increase in ranging performance will depend on the exact shape and placement of the GAL E1D signal. However, the impact of payload and receiver distortions has to be closely monitored and expected theoretical performance gains will be reduced significantly for realistic levels of distortion. NELP TOA estimation with a single signal (e.g., E1C only) is more robust with respect to distortions and can even perform better than a solution based on MSP of signals with an insufficient frequency offset, if the distortions are too severe.

Author Contributions: Conceptualization, F.C.B. and M.M.; methodology, F.C.B. and C.E.; software, F.C.B.; validation, F.C.B., C.E., and M.M.; formal analysis, F.C.B. and C.E.; investigation, F.C.B.; resources, F.C.B.; data curation, F.C.B. and S.T.; writing—original draft preparation, F.C.B.; writing—review and editing, F.C.B. and C.E.; visualization, F.C.B.; supervision, M.M.; project administration, S.T.; funding acquisition, M.M. All authors have read and agreed to the published version of the manuscript.

Funding: This research received no external funding.

Institutional Review Board Statement: Not applicable.

Informed Consent Statement: Not applicable.

Data Availability Statement: The data presented in this study are available upon request from the corresponding author.

Conflicts of Interest: The authors declare no conflict of interest.

References

1. García-Molina, J.A.; Wallner, S.; Vazquez, C.; De Pasquale, G.; Del Peral-Rosado, J.A.; Da Broi, G.; Schmitt, T.; Melman, F.; Parro, J.M.; Soualle, F.; et al. Quasi-Pilot Signals: Acquisition and Fast Time Ambiguity Resolution. In Proceedings of the 2022 10th Workshop on Satellite Navigation Technology (NAVITEC), Noordwijk, The Netherlands, 5–7 April 2022.
2. Paonni, M.; Bavaro, M. On the Design of a GNSS Acquisition Aiding Signal. In Proceedings of the 26th International Technical Meeting of The Satellite Division of the Institute of Navigation (ION GNSS+ 2013), Nashville, TN, USA, 16–20 September 2013; pp. 1445–1456.
3. Wallner, S.; García-Molina, J.A.; Hahn, J.; Risueno, G.L.; Broi, G.d.; Floch, J.J.; Soualle, F.; Schmitt, T.; Ouedraogo, M.; Wörz, T.; et al. Quasi-Pilot Signal Design-Facilitating New Signal Processing Concepts. In Proceedings of the 34th International Technical Meeting of the Satellite Division of The Institute of Navigation (ION GNSS+ 2021), St. Louis, MO, USA, 20–24 September 2021; pp. 1859–1876. [CrossRef]
4. Anghileri, M.; Floch, J.J.; Margaria, D.; Motella, B.; Peña, A.G.; Julien, O.; Macabiau, C.; Chauvat, R.; Paonni, M. FUNTIMES–Future Navigation and Timing Evolved Signals. In Proceedings of the 31st International Technical Meeting of the Satellite Division of the Institute of Navigation (ION GNSS+ 2018), Miami, FL, USA, 24–28 September 2018; pp. 876–912. [CrossRef]
5. Sénant, E.; Gadat, B.; Charbonnieras, C.; Roche, S.; Aubault, M.; Marmet, F.X. Tentative New Signals and Services in Upper L1 and S Bands for Galileo Evolutions. In Proceedings of the 31st International Technical Meeting of The Satellite Division of the Institute of Navigation (ION GNSS+ 2018), Miami, FL, USA, 24–28 September 2018. [CrossRef]
6. Ortega Espluga, L. Signal Optimization for Galileo Evolution. Ph.D. Thesis, Institut National Polytechnique de Toulouse, Toulouse, France, 2019.
7. Issler, J.L.; Paonni, M.; Eissfeller, B. Toward centimetric positioning thanks to L-and S-Band GNSS and to meta-GNSS signals. In Proceedings of the 2010 5th ESA Workshop on Satellite Navigation Technologies and European Workshop on GNSS Signals and Signal Processing (NAVITEC), Noordwijk, The Netherlands, 8–10 December 2010; pp. 1–8. [CrossRef]
8. Paonni, M.; Curran, J.T.; Bavaro, M.; Fortuny-Guasch, J. GNSS Meta Signals: Coherently Composite Processing of Multiple GNSS Signals. In Proceedings of the 27th International Technical Meeting of the Satellite Division of the Institute of Navigation (ION GNSS+ 2014), Tampa, FL, USA, 8–12 September 2014; pp. 2592–2601.
9. Ortega, L.; Vilà-Valls, J.; Chaumette, E.; Vincent, F. On the Time-Delay Estimation Accuracy Limit of GNSS Meta-Signals. In Proceedings of the 2020 IEEE 23rd International Conference on Intelligent Transportation Systems (ITSC), Rhodes, Greece, 20–23 September 2020; pp. 1–6. [CrossRef]
10. Borio, D.; Gioia, C. Reconstructing GNSS Meta-signal Observations Using Side-Band Measurements. *NAVIGATION J. Inst. Navig.* **2023**, *70*, 1–7. [CrossRef]
11. Schwalm, C.; Enneking, C.; Thölert, S. Ziv-Zakai Bound and Multicorrelator Compression for a Galileo E1 Meta-Signal. In Proceedings of the 2020 European Navigation Conference (ENC), Dresden, Germany, 23–24 November 2020; pp. 1–9. [CrossRef]
12. Wang, C.; Cui, X.; Ma, T.; Zhao, S.; Lu, M. Asymmetric Dual-Band Tracking Technique for Optimal Joint Processing of BDS B1I and B1C Signals. *Sensors* **2017**, *17*, 2360. [CrossRef] [PubMed]
13. Borio, D.; Gioia, C. GNSS Meta-signals, Dual-Frequency Combinations and the Double Phase Estimator. In Proceedings of the 2022 International Technical Meeting of the Institute of Navigation, Long Beach, CA, USA, 25–27 January 2022; pp. 1015–1026. [CrossRef]
14. Zhang, W.; Yao, Z.; Lu, M. WHAT: Wideband High-Accuracy Joint Tracking Technique for BDS B1 Composite Signal. In Proceedings of the 2019 IEEE 9th International Conference on Electronics Information and Emergency Communication (ICEIEC), Beijing, China, 12–14 July 2019; pp. 178–182. [CrossRef]
15. Tian, Z.; Cui, X.; Liu, G.; Lu, M. LPRA-DBT: Low-Processing-Rate Asymmetrical Dual-Band Tracking Method for BDS-3 B1I and B1C Composite Signal. In Proceedings of the International Technical Meeting of the Institute of Navigation, Long Beach, CA, USA, 25–27 January 2022. [CrossRef]

16. Nardin, A.; Dovis, F.; Motella, B. Impact of non-idealities on GNSS meta-signals processing. In Proceedings of the 2020 European Navigation Conference (ENC), Dresden, Germany, 23–24 November 2020; pp. 1–8. [CrossRef]
17. Beck, F.C.; Enneking, C.; Thölert, S.; Antreich, F. Comparison of Constant and Non-constant Envelope Signals for Satellite Navigation. In Proceedings of the 2022 10th Workshop on Satellite Navigation Technology (NAVITEC), Noordwijk, The Netherlands, 5–7 April 2022; pp. 1–9. [CrossRef]
18. Enneking, C.; Beck, F.C.; Thölert, S.; Antreich, F. Transmit Pulse Shaping for 1-Bit GNSS Receivers. In Proceedings of the 2022 International Conference on Localization and GNSS (ICL-GNSS), Tampere, Finland, 7–9 June 2022; pp. 1–6. [CrossRef]
19. Betz, J.W.; Goldstein, D.B. Candidate designs for an additional civil signal in GPS spectral bands. In Proceedings of the 2002 National Technical Meeting of the Institute of Navigation, ION, San Diego, CA, USA, 28–30 January 2002; pp. 622–631.
20. Teunissen, P.J.G.; Montenbruck, O. *Springer Handbook of Global Navigation Satellite Systems*; Springer: Berlin/Heidelberg, Germany, 2017.
21. Betz, J.W. *Engineering Satellite-Based Navigation and Timing: Global Navigation Satellite Systems, Signals, and Receivers*; John Wiley & Sons, Inc.: Hoboken, NJ, USA, 2015. [CrossRef]
22. Smith, J.O. Spectral Audio Signal Processing. Availiable online: https://ccrma.stanford.edu/~jos/sasp/ (accessed on 25 April 2023).